www.sciencemag.org/content/346/6209/617/suppl/DC1

Supplementary Materials for

A large magmatic sill complex beneath the Toba caldera

K. Jaxybulatov, N. M. Shapiro,* I. Koulakov, A. Mordret, M. Landès, C. Sens-Schönfelder

*Corresponding author. E-mail: nshapiro@ipgp.fr

Published 31 October 2014, *Science* **346**, 617 (2014)
DOI: 10.1126/science.1258582

This PDF file includes:

Materials and Methods
Figs. S1 to S10
Table S1
References (*32*–*43*)

Materials and Methods:

Observation of the crustal seismic anisotropy below the Toba caldera from the ambient noise seismic surface-wave tomography

We used six months of continuous records from the stations shown in Fig. 1. The stations were equipped with the 1 Hz Mark Products L-4 sensors whose lower-frequency limit of sensitivity is approximately at 0.06 Hz (*32*). We did not perform any instrumental correction, because all of the stations were equipped with similar instruments. We down-sampled the signals from 100 Hz to 10 Hz. Then, spectral whitening between 0.025 Hz and 5 Hz followed by one-bit normalization was applied to one-day records (*26,33*). Finally, we computed one-day cross-correlations between all pairs of stations, and stacked these over the whole six-month period. We used five components of the cross-correlation tensor: N-N, E-E, N-E, E-N, and Z-Z, and rotated these to transverse and radial components (*34*) (T-T, R-R, T-R, R-T) (Fig. S1). We used Frequency-Time analysis (*35,36*) to measure group velocities at periods between 3 s and 19 s (Fig. S2). The Z-Z and the R-R cross-correlations were used for Rayleigh waves and the T-T cross-correlations we used for Love waves (Fig. S1).

Reliable dispersion curves were selected according to the following criteria: 1) an inter-station distance more than 1.5 wavelengths; 2) a signal-to-noise ratio >1; 3) deviation of the group velocity from the average ≤50%; and 4) difference between group velocities measured from the positive and negative sides of the cross-correlations ≤100 m/s. The total numbers of retained dispersion curves for T-T, R-R and Z-Z components were 494, 440 and 585, respectively (Fig. S3). Finally, we smoothed the measured dispersion curves via applying a 4th order polynomial interpolation. The measurements from the Z-Z and the R-R components for every pair of stations were combined together.

We performed 2D tomographic inversions of the measured dispersion curves to construct the 2D group velocity maps at a set of periods (between 3 s and 19 s, with a step of 1 s; see examples in Fig. 2). We used a tomographic method based on a straight-ray approximation that minimizes a combination of a least-squares misfit function with regularization and smoothing terms (*27*). The

dispersion maps were parameterized on a grid with a regular spacing of 0.05°. This resulted in ray coverage with at least 5 rays per cell across most of the studied area (Fig. S4). The smoothing and damping parameters were selected to optimize the trade-off between the map smoothness and the variance reduction.

Regionalized dispersion curves at every grid point were inverted into local 1D shear velocity/ depth models using a Monte-Carlo method (random exploration of the model-parameters space) based on the Neighborhood Algorithm (*28,37*). We parameterized the model as a 1D S-wave depth/ velocity profile with 20 layers linearly spaced (see Figs. S6-S8). The depth and velocity of the first (Vs1, D1) and the last (Vs2, D2) layers with velocities of the other layers were inverted simultaneously. We imposed *a-priori* ranges of possible values for isotropic shear speeds and depths in the first and the last layers (based on inference from previous seismological studies): 1,500 m/s < Vs1 < 3,000 m/s; 100 m < D1 < 1,000 m; 3,800 m/s < Vs2 < 4,300 m/s; 29 km < D2 < 40 km. The shear speed ranges in the remaining 18 layers were defined from a condition that the difference between neighboring layers should not exceed 200 m/s. The values of the P-wave velocities and densities were computed from Vs via a simple scaling relation (*38*). Depth sensitivity kernels of the measured group velocities are shown in Fig. S5.

We first inverted the dispersion curves with a fully isotropic parameterization. The results are shown in Fig. S6. and demonstrate that in many locations, especially within the Toba caldera, the isotropic crustal structure cannot explain the Rayleigh and the Love wave dispersion curves simultaneously.To define an appropriate parameterization that allows for radial anisotropy, we first defined the average Rayleigh and Love wave dispersion curves for cells within the caldera where the isotropic inversion gave bad results (Misfit >0.4; Fig. S6a, black points). Then we inverted these average dispersion curves with a set of anisotropic parameterizations, as shown in Fig. S7. All of the models included a mid-crustal layer with a positive radial anisotropy ($V_{SH} > V_{SV}$), and we varied the upper limit of this layer. We also tested a set of models where we added a negative radial anisotropy in the top part of the crust. As can be seen in Fig. S7, the best result was obtained with a parameterization with a negative radial anisotropy (in the shallow part of the crust [layers 1 to 3] and a positive radial anisotropy in the middle crust below [layers 6 to 15]). Therefore, we introduced two additional parameters into our final inversion that described the radial anisotropy (*39*). These two parameters ξ_1 and ξ_2 describe the levels of radial anisotropy in layers 1-3 and 6-15, respectively ($\xi_I = 2*100\%*(V_{SH}–V_{SV})/(V_{SH}+V_{SV})$; $-15\% < \xi_1 < 0$; $0 < \xi_2 < 20\%$). To produce the final 3D model, we applied this new anisotropic parameterization to all of the points where the misfit after the isotropic inversion >0.2. For computing dispersion curves, we considered separate models for the SV and the SH cases and used the Computer Programs in Seismology package (*40*).

Finally, the inversion provided more than 25,000 1D models with different misfits at every grid point. The final 3D model of S-wave velocities in the crust beneath Toba caldera was calculated by averaging 1,000 best-fit solutions and by combining the averaged 1D profiles from all of the grid points (Fig. S9 and Fig. 3). A significant negative radial anisotropy was observed above 5 km, and mainly in the vicinity of the Sumatra fault and of the borders of the Toba Caldera, where vertically oriented structures are expected. The strongest anisotropy was negative and was observed below Samosir Island in the middle crust.

Analysis of the lateral resolution (*27*) of the group velocity dispersion maps (Fig. S10) indicated that anomalies larger than 20 km should be well resolved over the whole studied area. Vertically, the model was well resolved down to 20 km (below which the uncertainties increase

significantly). This implies that the radial anisotropy anomaly below the Toba caldera (Fig. 3) is well resolved. We also performed additional tests that showed that this anomaly was very robust with respect to the choice of the smoothing and damping parameters used in the construction of the group velocity maps, and with respect to the parameterization of the 1D shear velocity profiles. Independent of the choice of these different parameters, the explanation of the observations requires strong radial anisotropy below the Toba caldera at depths below 7 km.

Modeling radial anisotropy in the horizontally layered media

We modeled the structure of a layered intrusion as a 1D medium represented by a stack of n horizontal layers of total thickness H. When the wavelength $\boldsymbol{\lambda}$ is larger than the typical scale of vertical heterogeneity ***l'***, the propagation of elastic waves in such stack of layers can be approximated by an effective transversely isotropic (TI) media with a vertical axis of symmetry (*15*).

In our case, this condition was satisfied because the wavelengths were larger than 5 km and the typical scale of the vertical heterogeneity did not exceed a few hundreds of meters. A TI-media can be characterized by four types of waves, according to their propagation direction and polarization: ***qp1***, a quasi P-wave that propagates parallel to the symmetry axis (also known as ***PV***); ***qp2***, a quasi P wave that propagates perpendicularly to the symmetry axis; ***SH***, an S wave polarized in a direction perpendicular to the symmetry axis; and ***SV***, an S wave polarized in the direction parallel to the symmetry axis. A TI media is fully described by 5 elastic parameters: the speeds of the four described waves and by an additional parameter η. These parameters can be evaluated by averaging of the elastic properties of the media (*15*). In this study, we focus on three seismic speeds:

$$V_{PV} = \sqrt{\frac{\left\langle \frac{1}{\lambda + 2\mu} \right\rangle^{-1}}{\langle \rho \rangle}}, \qquad V_{SH} = \sqrt{\frac{\langle \mu \rangle}{\langle \rho \rangle}}, \qquad V_{SV} = \sqrt{\frac{\left\langle \frac{1}{\mu} \right\rangle^{-1}}{\langle \rho \rangle}} \qquad \text{(S1)},$$

where the averaging $\langle \cdot \rangle$ is calculated as: $\langle a \rangle = \sum_{1}^{n} a_i \cdot (h_i / H)$.

We generated sets of random 1D media with different average layer thicknesses and speeds. In all of the cases, the total thickness of the stack of the layers ***H*** was set to 15 km. For every tested set of parameters, we generated 1,000 1D models with random distributions of layer thicknesses and elastic parameters. The elastic modulus and density ($\boldsymbol{l_i}$,$\boldsymbol{m_i}$,$\boldsymbol{r_i}$,) of each layer were evaluated as follows (*38*):

$$V_{pi} = 1.73 \cdot V_{si}, \qquad \rho_i = \frac{V_{pi} + 2370}{1000 \cdot 2.81}, \qquad \mu_i = \rho_i V_{si}^2, \qquad \lambda_i = \rho_i V_{pi}^2 - 2\mu_i \qquad \text{(S2)},$$

where velocities are in ***m/s*** and densities are in ***kg/m^3***. The average layer thicknesses were controlled by the number of layers ***n***. We considered three values: ***n=100***, ***n=1,000***, and ***n=10,000***. We also tested the different levels of velocity contrast between the layers. In the first set of models (type of layers 1 in Table S1) only the extreme values $V_{si}=V_{min}$ and $V_{si}=V_{max}$ were assigned. In the second set (type of layers 2 in Table S1), V_{si} was distributed in intervals [V_{min} , $V_{min}+\delta V$] and [$V_{max}-\delta V$, V_{max}], where $\delta V = 0.1(V_{max}- V_{min})$. In the last set of models (type of layers 3 in Table S1), the values of V_{si} we homogenously distributed between V_{min} and V_{max}.

We compared the modeling results with the average shear wave speeds V_{SV} and V_{SH} observed below the Toba caldera at depths between 7 and 20 km. We estimated three sets of values by averaging all points with the radial anisotropy exceeding 5%, 7%, and 10%, respectively (Table S1). We also used the regional tomographic model based on records from earthquakes mainly located below the Toba caldera (*24*) (i.e., on nearly vertical rays) to deduce an average speed of vertically propagating P-waves V_{PV}. For the comparison, we selected from every set of 1000 models the one predicting better the observed values.

First, we tested the random media with velocities that varied within typical limits for the middle crust: V_{min} = ***3,000 m/s*** (Andesite) and V_{max} = ***3,800 m/s*** (Gabbro)[29]. The data presented in Table S1 show that for this range of velocities, the predicted values of the radial anisotropy are systematically lower, and the predicated seismic velocities are systematically higher, than the observations. Further tests showed that the observations can be reasonably predicted with the lower value of V_{min} = ***2,500 m/s***. Such low velocities can be explained either by rock with a strongly felsic composition, such as rhyolits (*30,38,41,42*), or more likely by a significant fraction of melt in some of the sills (2).

Overall, the modeling data show that the radial anisotropy is only weakly sensitive to the average thickness of the layers (sills), which, therefore, cannot be constrained from our observations. In contrast, the parameters that strongly affect the radial anisotropy are in the range of seismic speeds in the layers and the contrast between them. The explanation of the observed strong radial anisotropy requires a structure where the partially molten sills are emplaced between layers with fast seismic velocities that are typical for the middle crust.

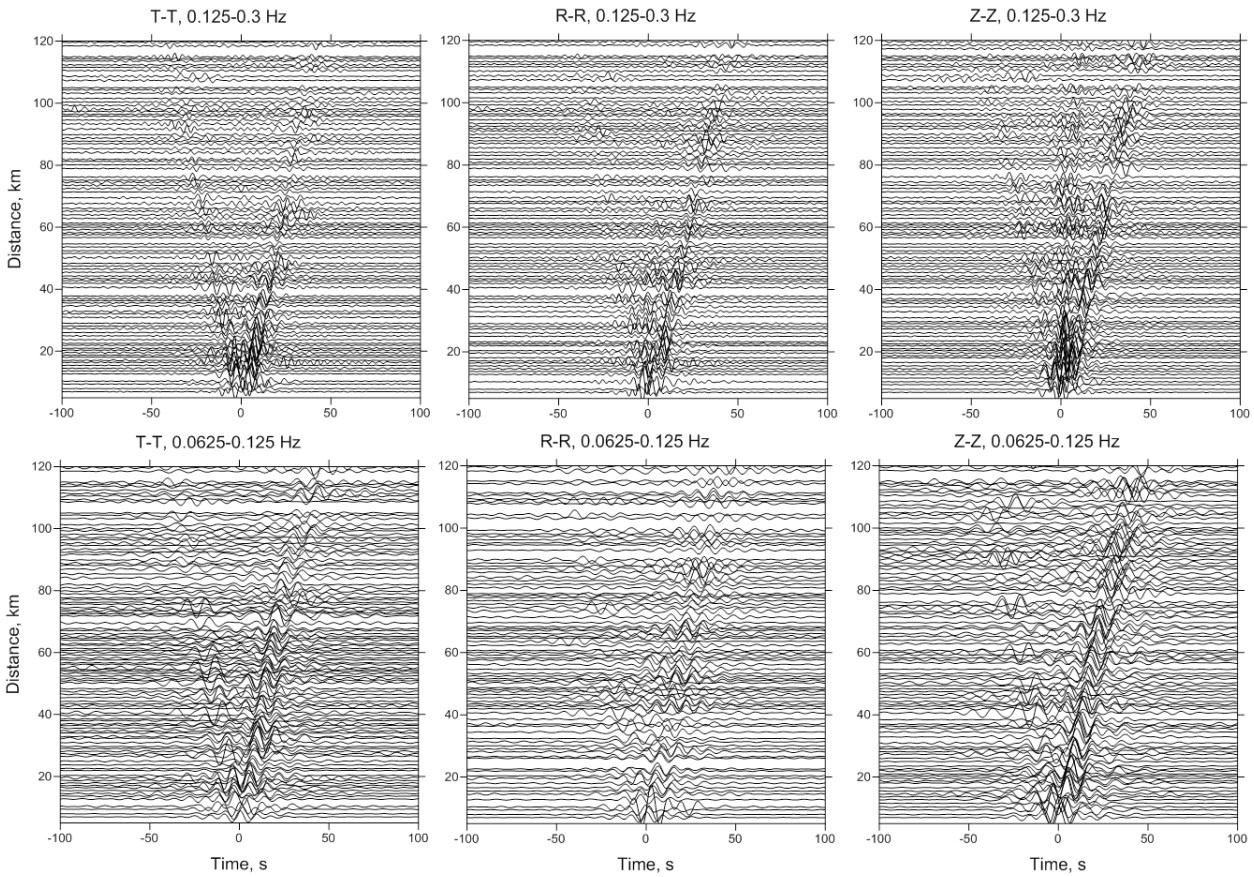

Fig. S1. Cross-correlations for all pairs of stations plotted as a function of inter-station distance (transverse, radial, and vertical components are indicated as T-T, R-R, and Z-Z, respectively). Waveforms were filtered in two frequency bands: 0.125-0.3 Hz and 0.0625-0.125 Hz. Energy arriving at near-zero times on the short-period R-R and Z-Z cross-correlations corresponds to teleseismic P-waves generated by a localized noise source in the South-Indian Ocean (*43*).

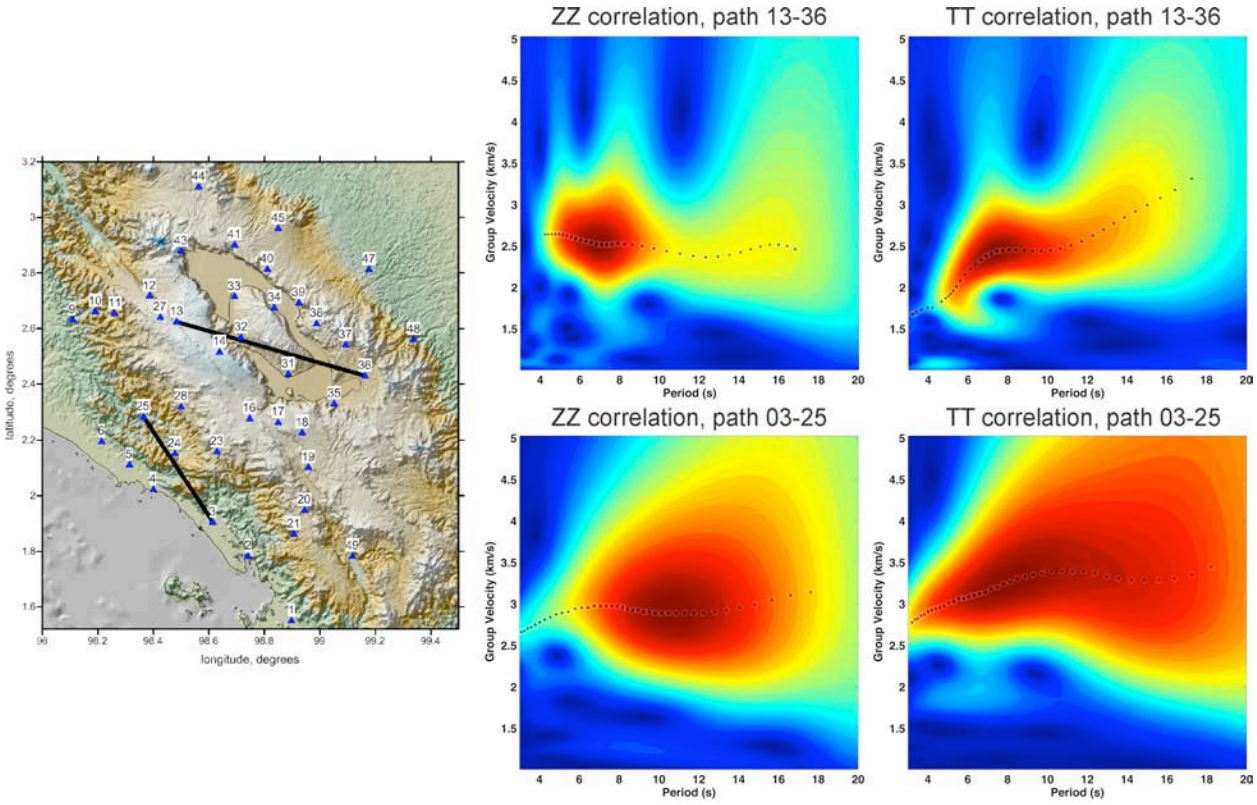

Fig. S2. Examples of the Frequency-Time Analysis (FTAN). Map on the left shows location of the selected station pairs. Amplitudes of the FTAN diagrams are shown with colors progressively increasing from dark blue to dark red. Small circles show measured dispersion curves.

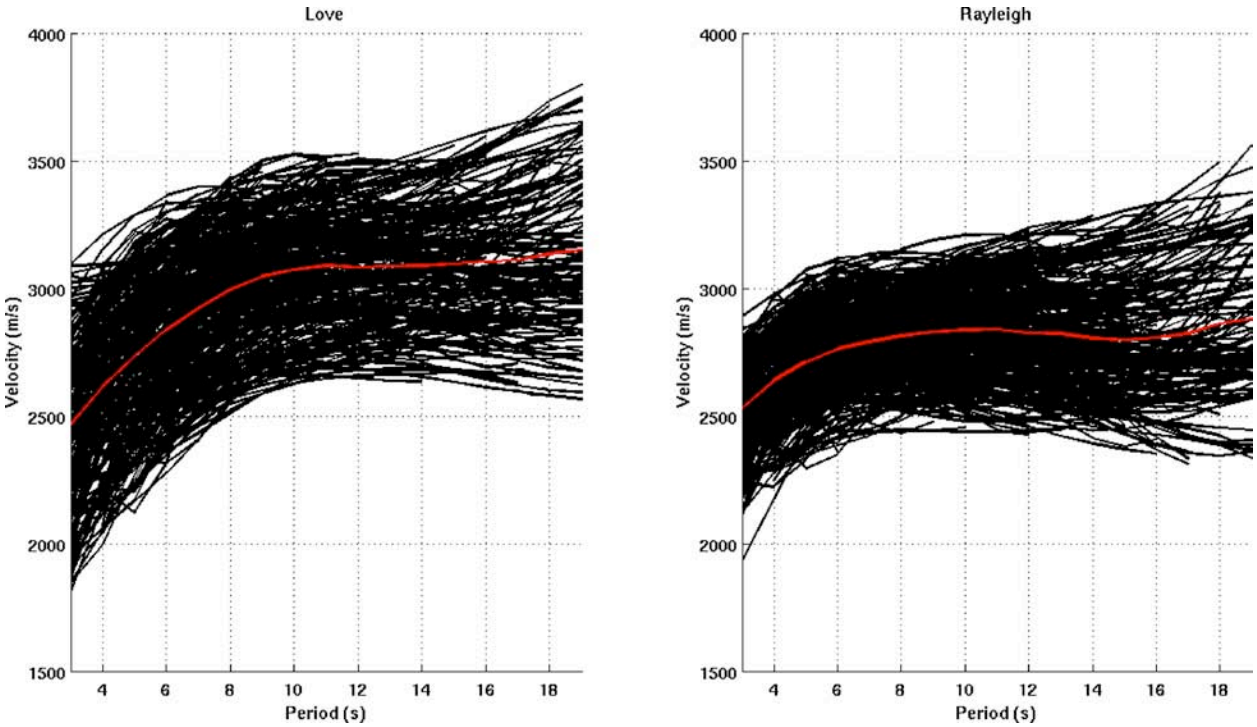

Fig. S3. All dispersion curves measured for Rayleigh and Love waves. Black lines show measurements from individual station pairs and red lines show average values.

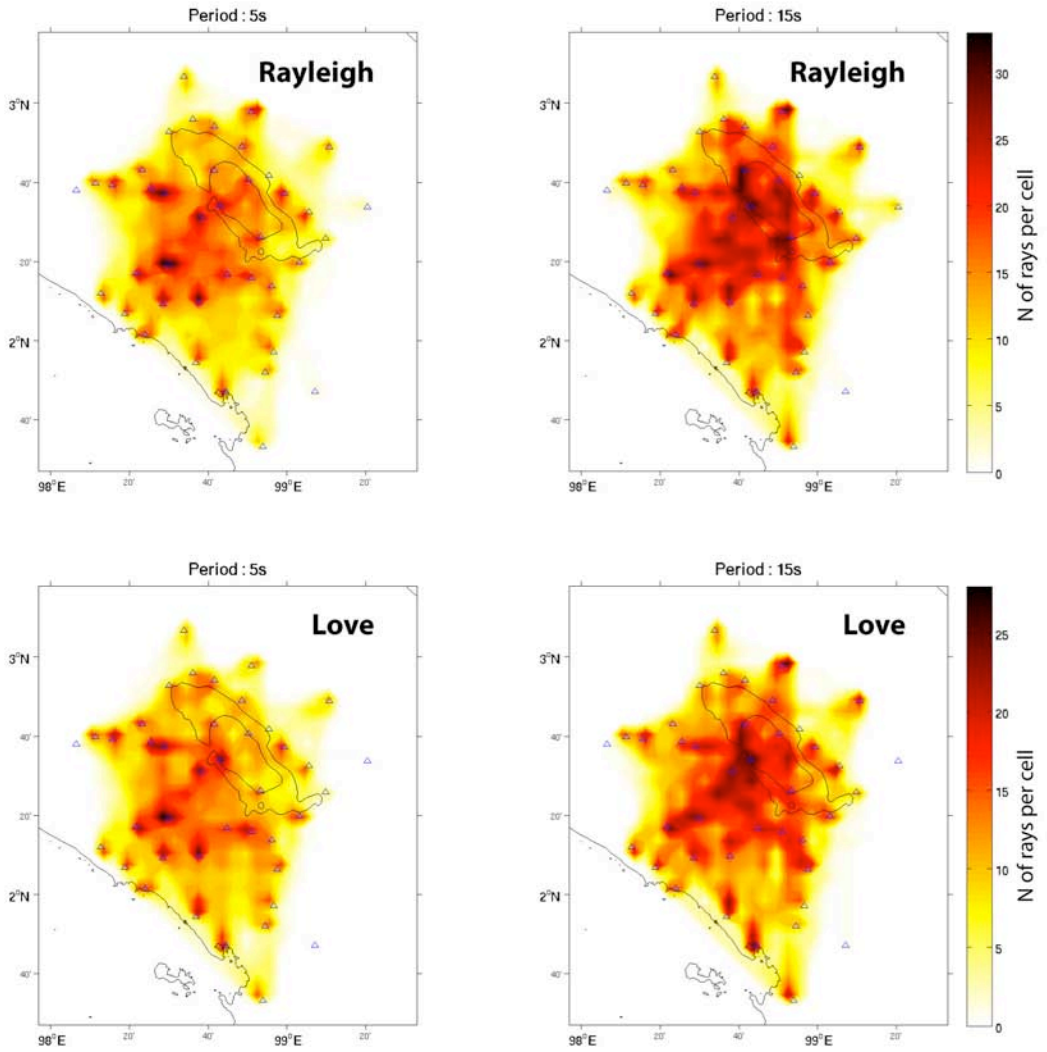

Fig. S4. Distribution of path density for Rayleigh and Love waves at periods of 5 and 15 s.

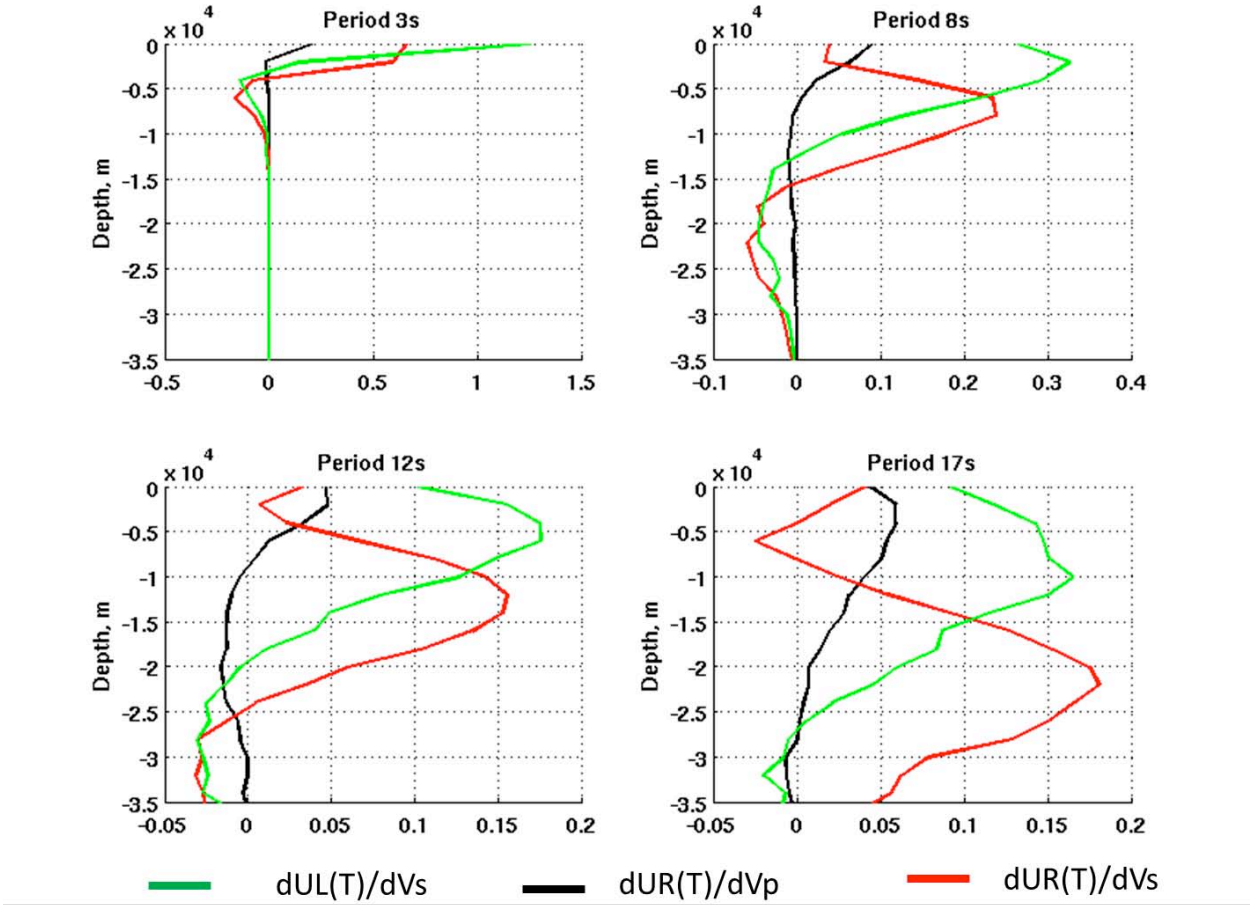

Fig. S5. Depth sensitivity kernels for Rayleigh (relative to Vs and Vp) and Love (relative to Vs) group velocities denoted UR and UL, respectively. Computation was performed at a set of periods with using a typical 1D isotropic structure of the Toba lake region.

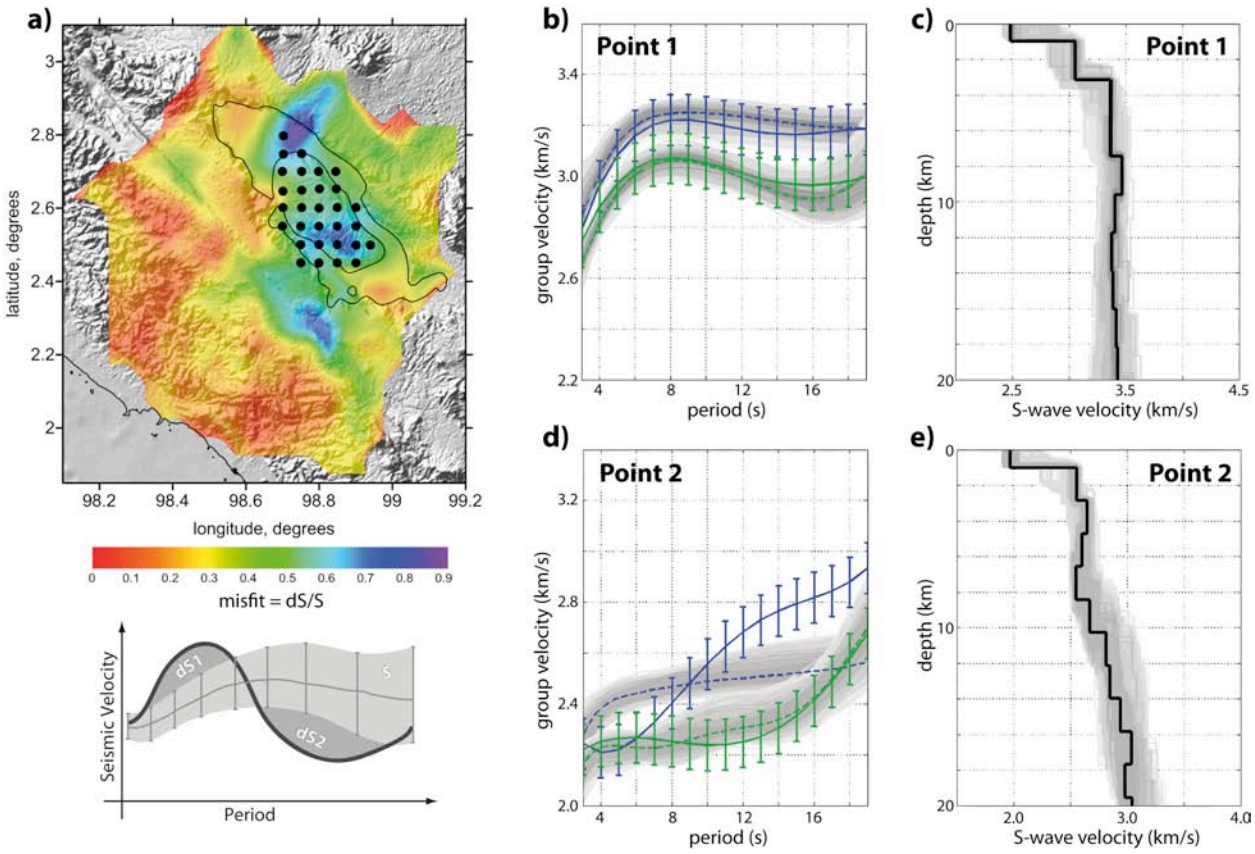

Fig. S6. Results of the inversion of dispersion curves based on isotropic parameterization. (a) Map of the misfit defined as the dimensionless ratio of the area of the predicted dispersion curve outside the area defined by the measured dispersion curve and its uncertainties, normalized by the area within one standard deviation of the measured dispersion curve (28) (as shown in the schematic illustration below the map). Black dots, grid points within the caldera where the misfit >0.4. Examples of 1D inversions of dispersion curves in points 1 and 2 shown in Fig. 1 are illustrated in (b, c) and (d, e), respectively. (b, d) Observed and predicted dispersion curves with solid and dashed lines, respectively (blue for Love waves, green for Rayleigh waves). Error bars of 200 m/s are estimated as average standard deviations of group velocity measurements. Grey lines, dispersion curves predicted from 1,000 best-fitting 1D profiles (darker colors correspond to better misfits). (c, e) Predicted shear velocity profiles. The best-fitting isotropic 1D profiles are shown with thick solid lines.

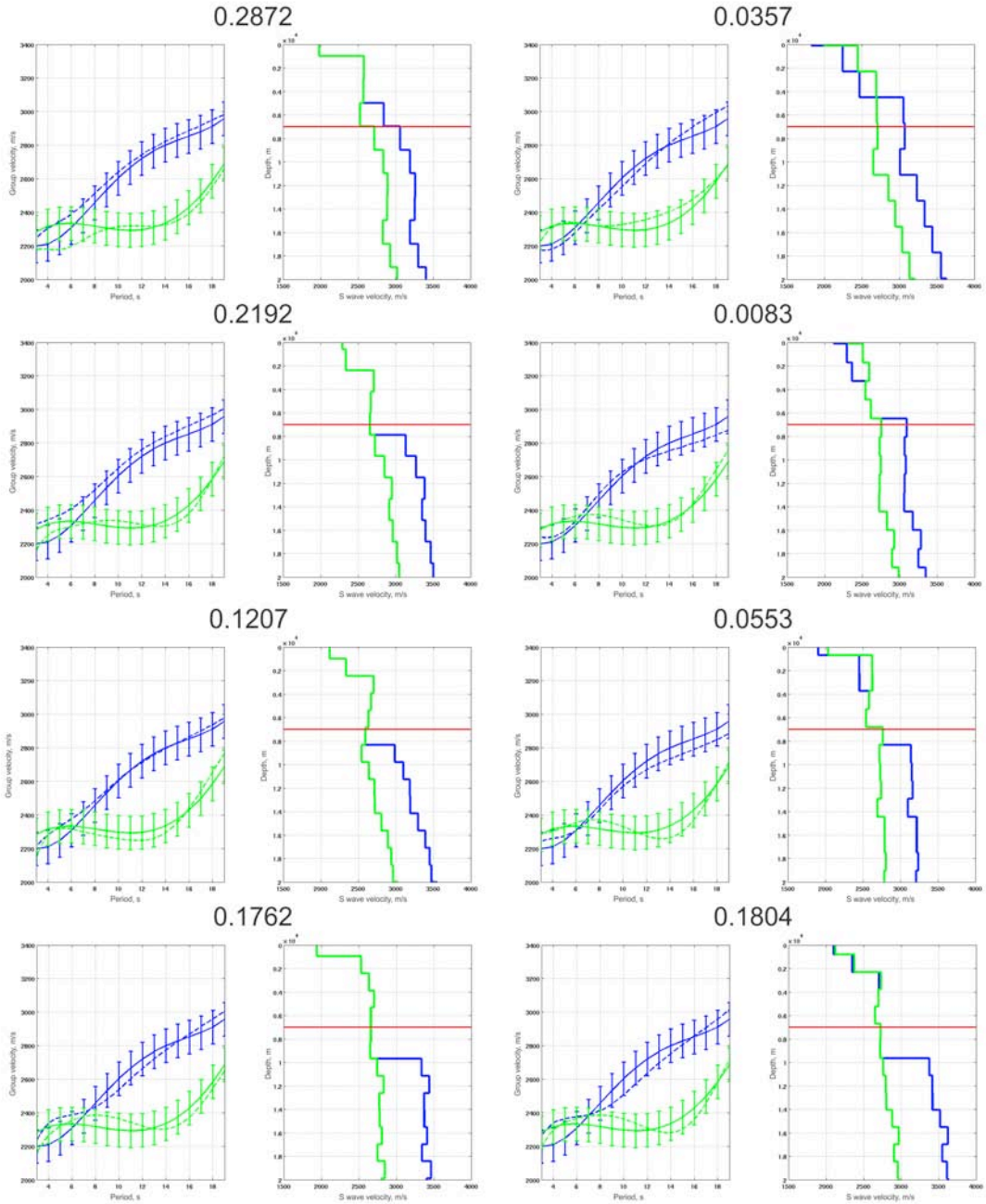

Fig. S7. One-dimensional inversions to test the anisotropic model parameterization. Left panel pairs: Solid lines, dispersion curves averaged over the areas indicated by the black points in Fig. S8a (Rayleigh and Love waves are shown in green and blue, respectively); dashed lines, dispersion curves predicted from the best-fit models shown in the right panels (V_{SV} and V_{SH} in green and blue, respectively); red line, 7 km in depth, for reference. The numbers on top are the misfits. The models on the left do not include anisotropy in the upper crust.

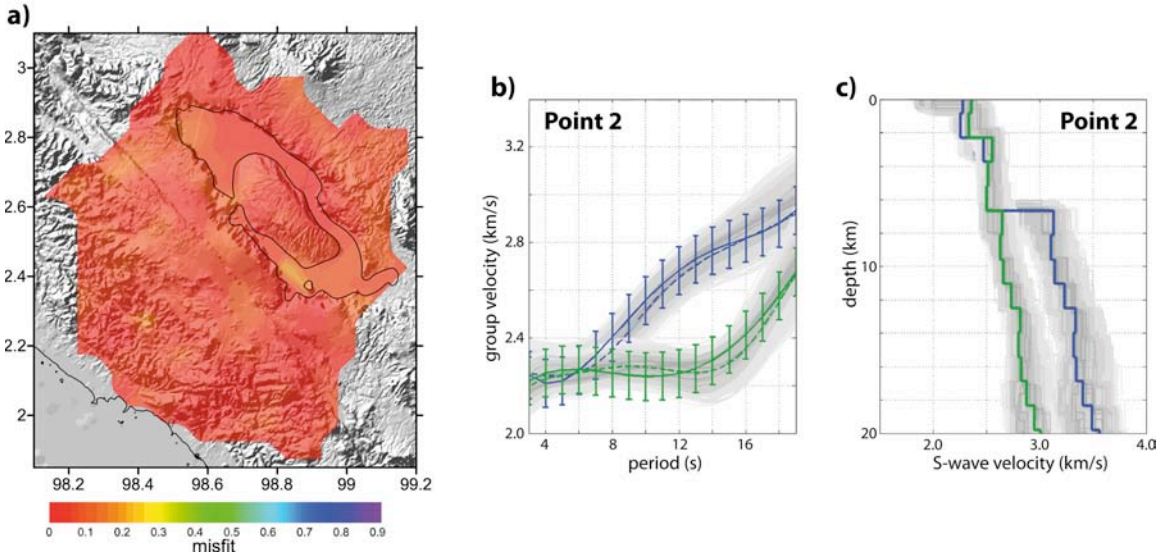

Fig. S8. Similar to Fig. S8 but for the combined model based on inversion with the isotropic and the anisotropic parameterizations.

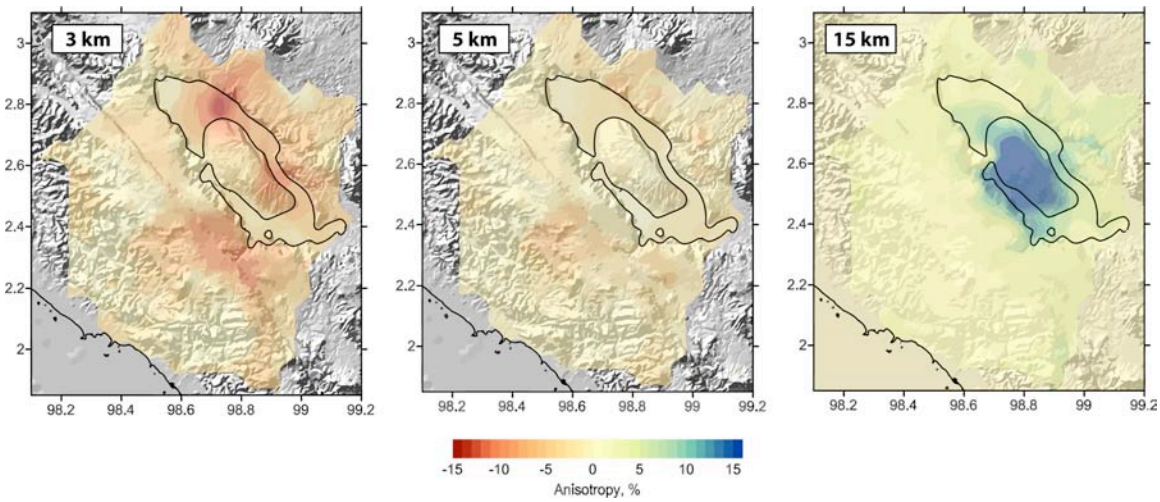

Fig. S9. Distributions of the radial anisotropy at 3 km, 5 km, and 15 km in depth.

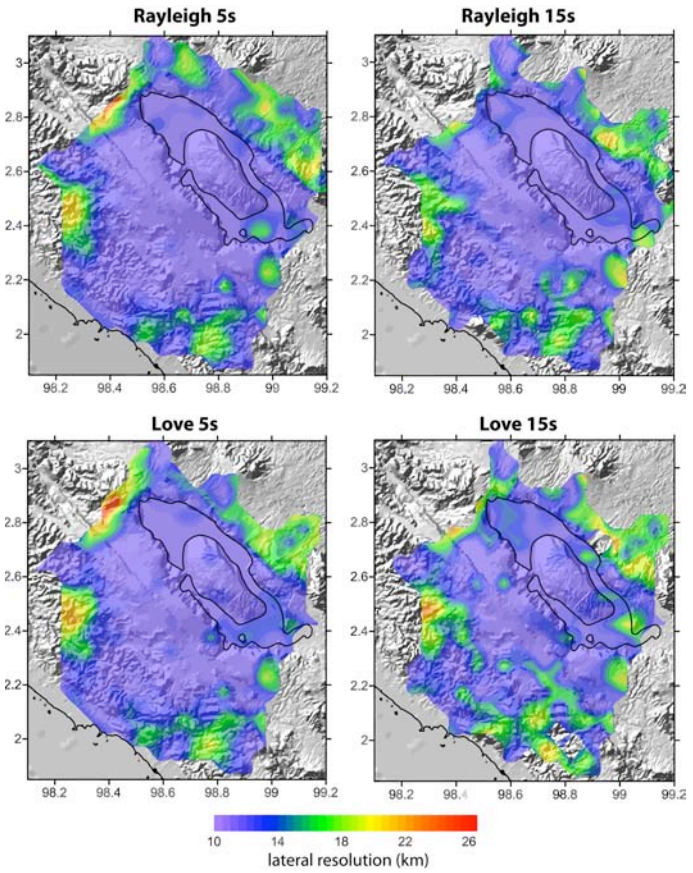

Fig. S10. Resolution analysis for the group velocity tomographic maps.

	V_{PV} (m/s)	V_{SH} (m/s)	V_{SV} (m/s)	ξ (%)
Observations				
From [1]	5300 ± 320			
From [2], for ξ > 5%		3390 ± 120	3100 ± 170	9.1 ± 3.8
From [2], for ξ > 7%		3370 ± 120	3010 ± 160	11.3 ± 3.5
From [2], for ξ > 10%		3350 ± 120	2920 ± 120	13.8 ± 2.5
Modeling: Vs=3000-3800 m/s				
Type of layers 1, N = 100	5642.9	3429.9	3261.8	5.03
Type of layers 2, N = 100	5695.9	3439.9	3292.5	4.37
Type of layers 3, N = 100	5717.2	3391.9	3304.7	2.60
Type of layers 1, N = 1000	5642.9	3429.9	3261.8	5.03
Type of layers 2, N = 1000	5711.6	3443.1	3301.5	4.20
Type of layers 3, N = 1000	5789.0	3412.5	3346.3	1.96
Type of layers 1, N=10000	5642.9	3429.9	3261.8	5.03
Type of layers 2, N=10000	5720.9	3446.7	3306.9	4.13
Type of layers 3, N=10000	5807.4	3417.4	3356.9	1.78
Modeling: Vs=2500-3800 m/s				
Type of layers 1, N=100	4918.6	3306.6	2843.1	15.07
Type of layers 2, N=100	4914.2	3243.1	2840.5	13.23
Type of layers 3, N=100	5190.5	3250.7	3000.3	8.01
Type of layers 1, N=1000	4918.6	3306.6	2843.1	15.07
Type of layers 2, N=1000	5002.5	3280.0	2891.6	12.59
Type of layers 3, N=1000	5258.3	3225.3	3039.5	5.93
Type of layers 1, N=10000	4918.6	3306.6	2843.1	15.07
Type of layers 2, N=10000	5007.1	3278.1	2894.3	12.43
Type of layers 3, N=10000	5243.4	3201.8	3030.9	5.48

Table S1. Comparison of the parameters of transversely isotropic media deduced from observations and from the modeling. The radial anisotropy was computed as: $\boldsymbol{\xi = 2*100\%*(V_{SH}-V_{SV})/(V_{SH}+V_{SV})}$.

References and Notes

1. O. Bachmann, G. Bergantz, The magma reservoirs that feed supereruptions. *Elements* **4**, 17–21 (2008).

2. C. Annen, J.-D. Blundy, R. S. J. Sparks, The genesis of intermediate and silicic magmas in deep crustal zones. *J. Petrol.* **47**, 505–539 (2006). doi:10.1093/petrology/egi084

3. C. Annen, From plutons to magma chambers: Thermal constraints on the accumulation of eruptible silicic magma in the upper crust. *Earth Planet. Sci. Lett.* **284**, 409–416 (2009). doi:10.1016/j.epsl.2009.05.006

4. C. A. Chesner, The Toba Caldera complex. *Quat. Int.* **258**, 5–18 (2012). doi:10.1016/j.quaint.2011.09.025

5. F. J. Gathorne-Hardy, W. E. H. Harcourt-Smith, The super-eruption of Toba, did it cause a human bottleneck? *J. Hum. Evol.* **45**, 227–230 (2003). Medline doi:10.1016/S0047-2484(03)00105-2

6. J. E. Gardner, P. W. Layer, M. J. Rutherford, Phenocrysts versus xenocrysts in the youngest Toba Tuff: Implications for the petrogenesis of 2,800 km^3 of magma. *Geology* **30**, 347–350 (2002). doi:10.1130/0091-7613(2002)030<0347:PVXITY>2.0.CO;2

7. C. Michaut, C. Jaupart, Two models for the formation of magma reservoirs by small increments. *Tectonophysics* **500**, 34–49 (2011). doi:10.1016/j.tecto.2009.08.019

8. A. Gudmundsson, Deflection of dykes into sills at discontinuities and magma-chamber formation. *Tectonophysics* **500**, 50–64 (2011). doi:10.1016/j.tecto.2009.10.015

9. B. Taisne, C. Jaupart, Dike propagation through layered rocks. *J. Geophys. Res.* **114**, B09203 (2009). 10.1029/2008JB006228 doi:10.1029/2008JB006228

10. G. J. Hill, T. G. Caldwell, W. Heise, D. G. Chertkoff, H. M. Bibby, M. K. Burgess, J. P. Cull, R. A. F. Cas, Distribution of melt beneath Mount St Helens and Mount Adams inferred from magnetotelluric data. *Nat. Geosci.* **2**, 785–789 (2009). doi:10.1038/ngeo661

11. J. M. Lees, Seismic tomography of magmatic systems. *J. Volcanol. Geotherm. Res.* **167**, 37–56 (2007). doi:10.1016/j.jvolgeores.2007.06.008

12. X. Peng, E. D. Humphreys, Crustal velocity structure across the eastern Snake River plain and the Yellowstone Swell. *J. Geophys. Res.* **103**, 7171–7186 (1998). doi:10.1029/97JB03615

13. J. W. Shervais, S. K. Vetter, B. B. Hanan, Layered mafic sill complex beneath the eastern Snake River Plain: Evidence from cyclic geochemical variations in basalt. *Geology* **34**, 365–368 (2006). doi:10.1130/G22226.1

14. I. Koulakov, A. Jakovlev, B. G. Luehr, A., Jakovlev, B. G., Luehr, Anisotropic structure beneath central Java from local earthquake tomography. *Geochem. Geophys. Geosyst.* **10**, Q02011 (2009). doi:10.1029/2008GC002109

15. G. W. Postma, Wave propagation in a stratified medium. *Geophysics* **20**, 780–806 (1955). doi:10.1190/1.1438187

16. G. Ekström, A. M. Dziewonski, The unique anisotropy of the Pacific upper mantle. *Nature* **394**, 168–172 (1998). doi:10.1038/28148

17. N. M. Shapiro, M. H. Ritzwoller, P. Molnar, V. Levin, Thinning and flow of Tibetan crust constrained by seismic anisotropy. *Science* **305**, 233–236 (2004). Medline doi:10.1126/science.1098276

18. M. P. Moschetti, M. H. Ritzwoller, F. Lin, Y. Yang, Seismic evidence for widespread western-US deep-crustal deformation caused by extension. *Nature* **464**, 885–889 (2010). Medline doi:10.1038/nature08951

19. Z. Wang, Seismic anisotropy in sedimentary rocks: Part 2—Laboratory data. *Geophysics* **67**, 1423–1440 (2002). doi:10.1190/1.1512743

20. N. M. Shapiro, M. Campillo, L. Stehly, M. H. Ritzwoller, High-resolution surface-wave tomography from ambient seismic noise. *Science* **307**, 1615–1618 (2005). Medline doi:10.1126/science.1108339

21. Information on materials and methods is available on *Science* Online.

22. Masturyono, R. McCaffrey, D. A. Wark, S. W. Roecker, Fauzi, G. Ibrahim, Sukhyar, Distribution of magma beneath the Toba caldera complex, north Sumatra, Indonesia, constrained by three-dimensional P-wave velocities, seismicity, and gravity data. *Geochem. Geophys. Geosyst.* **2**, 1014 (2001). doi:10.1029/2000GC000096

23. K. Sakaguchi, H. Gilbert, G. Zandt, G. and Zandt, Converted wave imaging of the Toba Caldera, Indonesia. *Geophys. Res. Lett.* **33**, L20305 (2006). doi:10.1029/2006GL027397

24. I. Koulakov, T. Yudistira, B. G. Luehr, P. Wandono, S velocity and Vp/Vs ratio beneath the Toba caldera complex (northern Sumatra) from local earthquake tomography. *Geophys. J. Int.* **177**, 1121–1139 (2009). doi:10.1111/j.1365-246X.2009.04114.x

25. J. Stankiewicz, T. Ryberg, C. Haberland, D. Fauzi, D. Natawidjaja, Natawidjaja, Lake Toba volcano magma chamber imaged by ambient seismic noise tomography. *Geophys. Res. Lett.* **37**, L17306 (2010). doi:10.1029/2010GL044211

26. G. D. Bensen, M. H. Ritzwoller, M. P. Barmin, A. L. Levshin, F. Lin, M. P. Moschetti, N. M. Shapiro, Y. Yang, Processing seismic ambient noise data to obtain reliable broadband surface wave dispersion measurements. *Geophys. J. Int.* **169**, 1239–1260 (2007). doi:10.1111/j.1365-246X.2007.03374.x

27. M. Barmin, M. H. Ritzwoller, A. L. Levshin, A fast and reliable method for surface wave tomography. *Pure Appl. Geophys.* **158**, 1351–1375 (2001). doi:10.1007/PL00001225

28. A. Mordret, M. Landès, N. M. Shapiro, S. Singh, P. Roux, Ambient noise surface-wave tomography to determine the shallow shear velocity structure at Valhall: Depth inversion with a Neighbourhood Algorithm. *Geophys. J. Int.* **198**, 1514–1525 (2014). doi:10.1093/gji/ggu217

29. T. M. Brocher, Compressional and shear-wave velocity versus depth relations for common rock types in northern California. *Bull. Seismol. Soc. Am.* **98**, 950–968 (2008). doi:10.1785/0120060403

30. K. Wohletz, G. Heiken, *Volcanology and Geothermal Energy* (Univ. of California Press, Berkeley, CA, 1992).

31. E. Chaussard, F. Amelung, Precursory inflation of shallow magma reservoirs at west Sunda volcanoes detected by InSAR. *Geophys. Res. Lett.* **39**, L21311 (2012). doi:10.1029/2012GL053817

32. M. A. Riedesel, R. D. Moore, J. Orcutt, Limits of sensitivity of inertial seismometers with velocity transducers and electronic amplifiers. *Bull. Seismol. Soc. Am.* **80**, 1725–1752 (1990).

33. P. Cupillard, L. Stehly, B. Romanowicz, The one-bit noise correlation: A theory based on the concepts of coherent and incoherent noise. *Geophys. J. Int.* **184**, 1397–1414 (2011). doi:10.1111/j.1365-246X.2010.04923.x

34. F. C. Lin, M. P. Moschetti, M. H. Ritzwoller, Surface wave tomography of the western United States from ambient seismic noise: Rayleigh and Love wave phase velocity maps. *Geophys. J. Int.* **173**, 281–298 (2008). doi:10.1111/j.1365-246X.2008.03720.x

35. A. L. Levshin, T. Yanovskaya, A. Lander, B. Bukchin, M. Barmin, L. Ratnikova, E. Its, *Seismic Surface Waves in a Laterally Inhomogeneous Earth*, V. I. Keilis-Borok, Ed. (Springer, New York, 1989).

36. N. M. Shapiro, S. K. Singh, A systematic error in estimating surface-wave velocity dispersion curves and a procedure for its correction. *Bull. Seismol. Soc. Am.* **89**, 1138–1142 (1999).

37. M. Sambridge, Geophysical inversion with a neighbourhood algorithm. I. Searching a parameter space. *Geophys. J. Int.* **138**, 479–494 (1999). doi:10.1046/j.1365-246X.1999.00876.x

38. H. Gebrande, H. Kern, F. Rummel, *Landolt-Börnstein Numerical Data and Functional Relationship in Science and Technology. Group V. Geophysics and Space Research, Physical Properties of Rocks*, Subvolume b, 1 (Springer-Verlag, Berlin, 1982).

39. J. Xie, M. H. Ritzwoller, W. Shen, Y. Yang, Y. Zheng, L. Zhou, Crustal radial anisotropy across Eastern Tibet and the Western Yangtze Craton. *J. Geophys. Res.* **118**, 4226–4252 (2013). doi:10.1002/jgrb.50296

40. R. B. Herrmann, C. J. Ammon, *Computer Programs in Seismology: Surface Waves, Receiver Functions and Crustal Structure* (St. Louis University, St. Louis, MO, 2002).

41. A. F. Woeber, S. Katz, T. J. Ahrens, Elasticity of selected rocks and minerals. *Geophysics* **28**, 658–663 (1963). doi:10.1190/1.1439242

42. N. I. Christensen, R. L. Carlson, M. H. Salisbury, D. M. Fountain, in *Initial Reports of the Deep Sea Drilling Project*, vol. XXXI, D. E. Karig, J. C. Ingle Jr., A. H. Bouma, C. H. Ellis, N. Haile, I. Koizumi, H. Yi Ling, I. MacGregor, J. C. Moore, H. Ujiie, T. Watanabe, S. M. White, M. Yasui, Eds. (report no. 607-610, U.S. Government Printing Office Washington, DC, 1975).

43. M. Landès, F. Hubans, N. M. Shapiro, A. Paul, M. Campillo, Origin of deep ocean microseisms by using teleseismic body waves. *J. Geophys. Res.* **115**, B05302 (2010). doi:10.1029/2009JB006918